

# Crystal structure of an RNA tertiary domain essential to HCV IRES-mediated translation initiation

Jeffrey S. Kieft<sup>1,2</sup>, Kaihong Zhou<sup>1,2</sup>, Angie Grech<sup>1</sup>, Ronald Jubin<sup>3</sup> and Jennifer A. Doudna<sup>1,2</sup>

<sup>1</sup>Department of Molecular Biophysics and Biochemistry and <sup>2</sup>Howard Hughes Medical Institute, Yale University, New Haven, Connecticut 06520-8114, USA. <sup>3</sup>Schering-Plough Research Institute, Kenilworth, New Jersey 07033-0539, USA.

Published online: 1 April 2002, DOI: 10.1038/nsb781

**The hepatitis C virus (HCV) internal ribosome entry site (IRES) RNA drives internal initiation of viral protein synthesis during host cell infection. In the tertiary structure of the IRES RNA, two helical junctions create recognition sites for direct binding of the 40S ribosomal subunit and eukaryotic initiation factor 3 (eIF3). The 2.8 Å resolution structure of the IIIabc four-way junction, which is critical for binding eIF3, reveals how junction nucleotides interact with an adjacent helix to position regions directly involved in eIF3 recognition. Two of the emergent helices stack to form a nearly continuous A-form duplex, while stacking of the other two helices is interrupted by the insertion of junction residues into the helix minor groove. This distorted stack probably serves as an important recognition surface for the translational machinery.**

Translation initiation in eukaryotes occurs by at least two distinct pathways (Fig. 1a). The mechanism used by the vast majority of eukaryotic messages requires recognition of a modified 5' terminal nucleotide on the mRNA, triggering binding of several multisubunit translation initiation factors that direct the ribosome to the translational start site<sup>1</sup>. Alternatively, some eukaryotic genes and viruses utilize a 5' end-independent mechanism, which involves direct entry of the translational machinery at or just upstream of the correct start codon<sup>2</sup>. An internal ribosome entry site (IRES) in the 5' untranslated region (UTR) of these mRNAs drives this mode of internal initiation through inter-actions between the IRES RNA and the translational machinery.

In hepatitis C virus (HCV), the ~340-nucleotide IRES sequence comprises nearly the entire 5' UTR<sup>3,4</sup>. Because the IRES RNA functionally replaces the eIF4F protein complex (eIF4E, eIF4G, eIF4A and eIF4B), ribosome recruitment in HCV requires just two of the canonical initiation factors necessary for cap-dependent initiation<sup>5</sup>. The IRES RNA, one of the most conserved regions of the entire HCV genome, directly and specifically binds the 40S ribosomal subunit and eukaryotic initiation factor 3 (eIF3)<sup>6-9</sup>. This complex, in concert with initiator tRNA, GTP and the associated initiation factor eIF2, forms the 48S preinitiation complex, which recruits the 60S ribosomal subunit to begin viral protein synthesis<sup>5</sup>.

The IRES RNA folds in the presence of physiological concentrations of metal ions into an extended scaffold-like tertiary structure that directly recruits the 40S subunit and eIF3 (ref. 10). This HCV IRES RNA structure has been analyzed using both cryo-electron microscopy (cryo-EM) and NMR. Cryo-EM com-

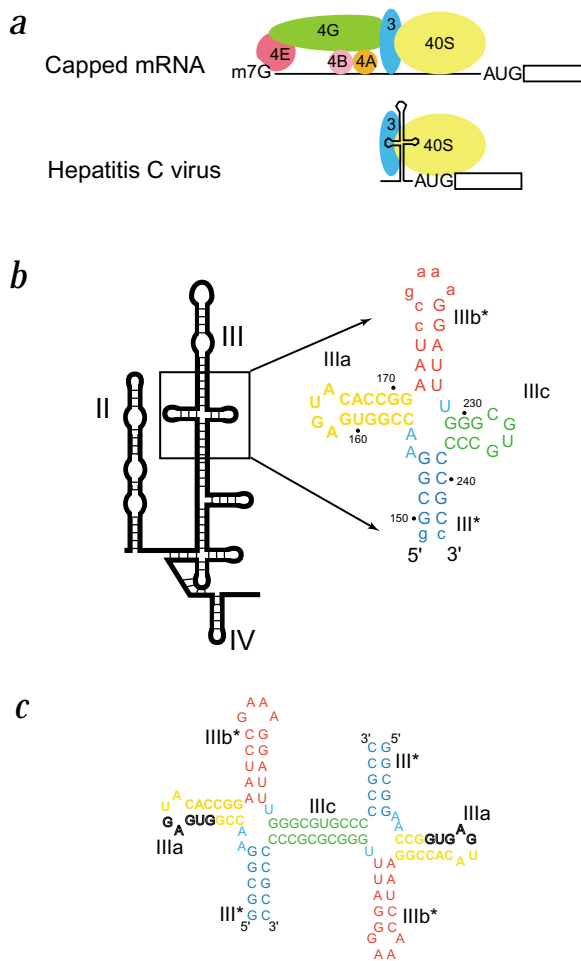


**Fig. 1** Function of the HCV IRES and design of the crystallization construct. **a**, Comparison of cap-dependent (top) and internal (bottom) translation initiation. In cap-dependent initiation, recruitment of the 40S subunit is driven by recognition of the modified nucleotide cap by the eIF4F complex. In HCV IRES driven internal initiation, the IRES RNA recruits the translation machinery directly. **b**, Secondary structure of the HCV IRES, showing the location of junction IIIabc and the design of the crystallization construct. Nucleotides that differ from the native sequence are designated in lowercase. **c**, Secondary structural diagram of the crystallization-induced dimer. Loop IIIa nucleotides for which no electron density was observed are shown in outline.

pared with the single-particle approach produced ~20 Å structures of the mammalian 40S ribosomal subunit in complex with either the wild type IRES or a deletion mutant lacking domain II<sup>11</sup> (Fig. 1b). These images revealed that IRES RNA binding induces a significant conformational change in the 40S subunit that requires domain II, demonstrating that the HCV IRES is a dynamic manipulator of the translational machinery. In addition, NMR has been used to solve the structures of isolated HCV IRES stem-loops IIIc and IIIe, providing insight into the details of RNA structures thought to directly contact the 40S subunit<sup>12,13</sup>.

Toe-printing, footprinting, quantitative binding assays and modification interference experiments showed that two folded four-way junctions in the IRES RNA create specific recognition sites for the 40S ribosomal subunit and eIF3 (refs 5,8,9). One junction comprises the core of the 40S subunit binding site and may play a critical role in positioning the translation start codon



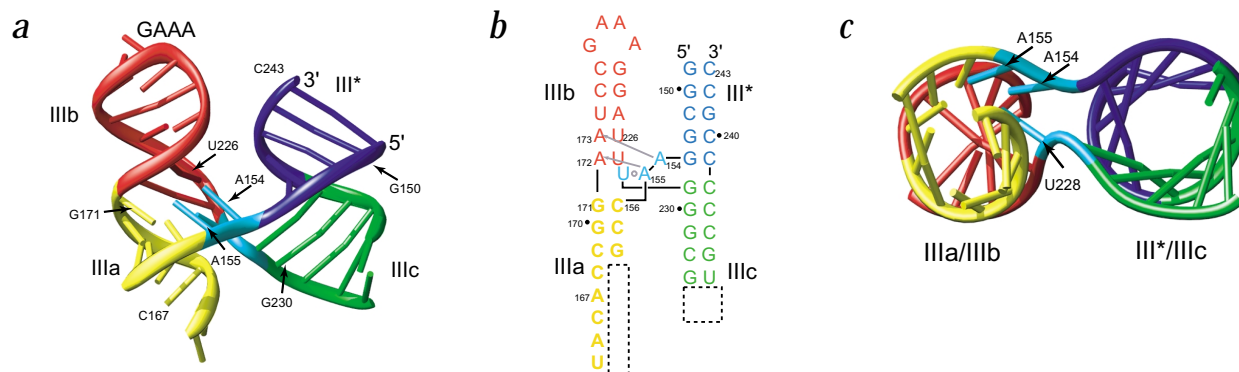


**Fig. 2** Three-dimensional structure of the four-way RNA junction. **a**, Overall structure of junction IIIabc from the HCV IRES RNA. Helix III\* is shown in blue, IIIc in green, IIIb and the GAAA tetraloop in red, and IIIa in yellow. The three single-stranded junction nucleotides are shown in cyan. Loop IIIc is missing due to RNA dimerization in the crystal (Fig. 1c). Loop IIIa is incomplete because this region is not structured in the crystal and these nucleotides were not visible in the electron density map. The two junction adenosines lie on the near side of the junction, pointing into the IIIa–b stack. **b**, Modified secondary structural diagram depicting the overall stacking geometry and tertiary interactions of junction IIIabc. The noncanonical base pair between U228 and A154 is indicated with a gray open circle, and the interactions of A154 and A155 with the minor groove of stem IIIb are shown with gray arrows. Dashed boxes indicate locations where loop IIIc is missing (right) due to dimerization or loop IIIa is missing (left) due to disorder in the crystal. **c**, View down the helical axis of the junction structure, with the GAAA loop removed for clarity. The III\*–IIIc stack (right) is nearly perfectly A-form, whereas the IIIa–b stack (left) is distorted; color scheme is the same as in Fig. 1b. Panels (a) and (b) were created using Ribbons<sup>25</sup>.

in the ribosomal P-site. The other junction connects helices IIIa, IIIb and IIIc to the remainder of domain III (Fig. 1b). This IIIabc junction lies at the interface of the 40S ribosomal subunit and eIF3 binding sites<sup>6,9,14</sup> and is critical for IRES RNA folding, assembly of the translational machinery and initiation of translation<sup>10,15</sup>. Point mutations within the junction reduce the binding affinity of the 40S subunit and eIF3 for the IRES RNA and severely decrease the efficiency of IRES-driven translation initiation<sup>9</sup>. Thus, the structural integrity of this junction is critical for HCV IRES biological activity.

To determine the structural basis for the importance of junction IIIabc in IRES function, we have solved its crystal structure at 2.8 Å resolution. The structure reveals two sets of stacked helices, one of which is distorted by the insertion of single-stranded residues within the junction into its minor groove. *In vitro* translation assays of IRES variants containing mutations that disrupt junction interactions suggest that this distorted helical structure is critical for correct placement of the translation machinery on the IRES RNA.

#### Junction IIIabc includes two helical stacks

To obtain diffraction quality crystals of junction IIIabc, the apical stem-loop and internal loop of domain IIIb were removed, the IIIb helix was capped with a GAAA tetraloop and the initial base pair was changed to a G–C (Fig. 1b). Enzymatic probing, mutagenesis and eIF3-binding assays were conducted with this truncated construct, and the results were compared to those for the intact HCV IRES RNA, as well as a 100-nucleotide RNA corresponding to the wild type IIIabc region from nucleotides 146–245. The partial T1 cleavage pattern of the crystallization construct in the presence of MgCl<sub>2</sub> is similar to that observed for the complete IIIabc region, as well as to the IIIabc junction within the intact IRES RNA<sup>10</sup> (data not shown). Introduction of a U228C mutation into the crystallization construct results in a smearing of the RNA band on a native gel, indicating destabilization of the junction similar to that observed when the same mutation is made in the intact IRES RNA (data not shown). This observation provides further evidence that the isolated junction behaves similarly to the IIIabc

junction within the full-length IRES RNA. These results indicate that the solution structures are similar in all cases, although the crystallization construct is unable to bind eIF3 because of the lack of required nucleotides in stem-loop IIIb<sup>5,6,9,14,15</sup>. Variation of the helical lengths in the truncated IIIabc RNA led to a construct that yielded crystals with a maximum diffraction limit of 2.8 Å. Heavy-atom derivatives for use in MAD phasing were obtained by 100% incorporation of 5-bromo-uracil during *in vitro* transcription<sup>16</sup>. Crystallization conditions and parameters were identical for native and brominated RNA, indicating that the bromine atoms did not alter the crystal structure. Dimerization of the RNA, which occurred during crystallization, eliminates loop IIIc but does not change the secondary structure of the junction (Fig. 1c). This RNA forms a monomer in solution regardless of the annealing protocol or RNA concentration, indicating that dimerization is a crystallization-induced strand exchange, as assayed by native gel electrophoresis (data not shown).

In the junction IIIabc structure, two coplanar sets of stacked helices produce an overall ‘X’ shape in which stem IIIa stacks on stem IIIb, and stem IIIc stacks on the remaining helix (referred to as stem III\*) (Fig. 2a,b). The two helical stacks connect at the junction in a parallel orientation *via* crossovers that consist of a single phosphate. Single-stranded junction nucleotides A154, A155 and U228 insert into the IIIa–IIIb interface, where they distort the overall stacking geometry (Fig. 2c). In contrast, the IIIc–III\* stack is almost perfectly coaxial and continuously A-form. Within the emerging helices, the secondary structure is as predicted.

The HCV IRES junction IIIabc shares topological similarities with an RNA structure within the 50S ribosomal subunit that joins helices 94, 95, 96 and 97 (J94–97)<sup>17</sup>. In both cases, adjacent junction adenosine nucleotides contact the minor groove of a distorted helical stack, and all four helices lie in a single plane in a parallel configuration. In the rRNA junction, the emergent helices interact closely with ribosomal proteins within the dense fold of the ribosome, suggesting a possible mode of interaction between the IIIabc junction and protein subunits of eIF3 (refs 14,18). In contrast, junction IIIabc is topologically distinct

from Holliday junctions, in which the sugar-phosphate backbones reverse direction as they pass through the junction in an antiparallel configuration<sup>19</sup>.

**Critical nucleotides organize the junction**

The junction is held together by a complex network of hydrogen bonds involving Watson-Crick base pairs, noncanonical base-base interactions and base-sugar interactions, which all reside in the interface between stem IIIa and IIIb (Fig. 3a). The internucleotide interactions are akin to a spiral staircase that can be traced continuously through U228→A155→A172-U227→A154→A173-U226 (where ‘-’ indicates Watson-Crick pairing in helix IIIb). A critical cross-junction interaction occurs between the Watson-Crick face of U228 and the major groove side of A155, with hydrogen bonds between U228 O4 and the exocyclic amine of A155. The formation of this cross-junction interaction is consistent with the observation that mutation of the U228 O4 carbonyl functional group to an amine (U to C) results in unfolding of the junction, loss of IRES RNA binding affinity for both the 40S subunit and eIF3, and loss of IRES translation initiation activity<sup>5,9</sup>. In addition, U228 N3 is within hydrogen bonding distance of A155 N7. The non-canonical cross-junction U228-A155 pair then interacts with the minor groove of the Watson-Crick A172-U227 pair in helix IIIb through the Watson-Crick face of A155 and the 2' hydroxyl and minor groove N3 of A172. U227 then makes several contacts with the second junction adenosine (A154) via hydrogen bonds between U227 O2 and the A154 exocyclic amine, and the U227 2' hydroxyl and A154 N7. A154 stacks on A155 and also

contacts the next Watson-Crick base pair in IIIb, A173-U226, through hydrogen bonds with A154 imino-A173 2' hydroxyl and A154 amine-A173 N3. Thus, both junction A nucleotides interact with adjacent A-U base pairs in the minor groove of IIIb using identical sets of contacts.

Disruption of the network of hydrogen bonds that knits the junction together is expected to disrupt the ability of the IRES to bind eIF3 and the ribosome and, consequently, to initiate translation of a downstream reporter gene. This effect has been observed with the U228C mutant described above. Based on the three-dimensional structure, we constructed a series of full-length IRES mutants that contain disruptions of various interactions within the junction and tested their translation initiation activity (Table 1). The junction nucleotide mutations A154G and A155G replace an exocyclic amine with a carbonyl group and, thus, should prevent these groups from forming the hydrogen bonds observed in the structure. Indeed, the A154G and A155G mutants both show a pronounced loss of translation initiation activity (1% and 3% of wild type, respectively). In addition to the junction nucleotides, the base pairs of helix IIIb adjacent to the junction are important contributors to the structure. Mutations A172U and A173U, in which an A-U base pair is changed to a U•U mismatch, alter the identity of the minor groove functional groups and destabilize the secondary structure of the helix. As expected, these mutants are severely inhibited in their ability to initiate translation (9% and 5% of wild type, respectively). Restoration of base pairing in the A172U and A173U mutants by a compensatory U227A or U226A mutation, respectively, restores translation initiation activity to near wild

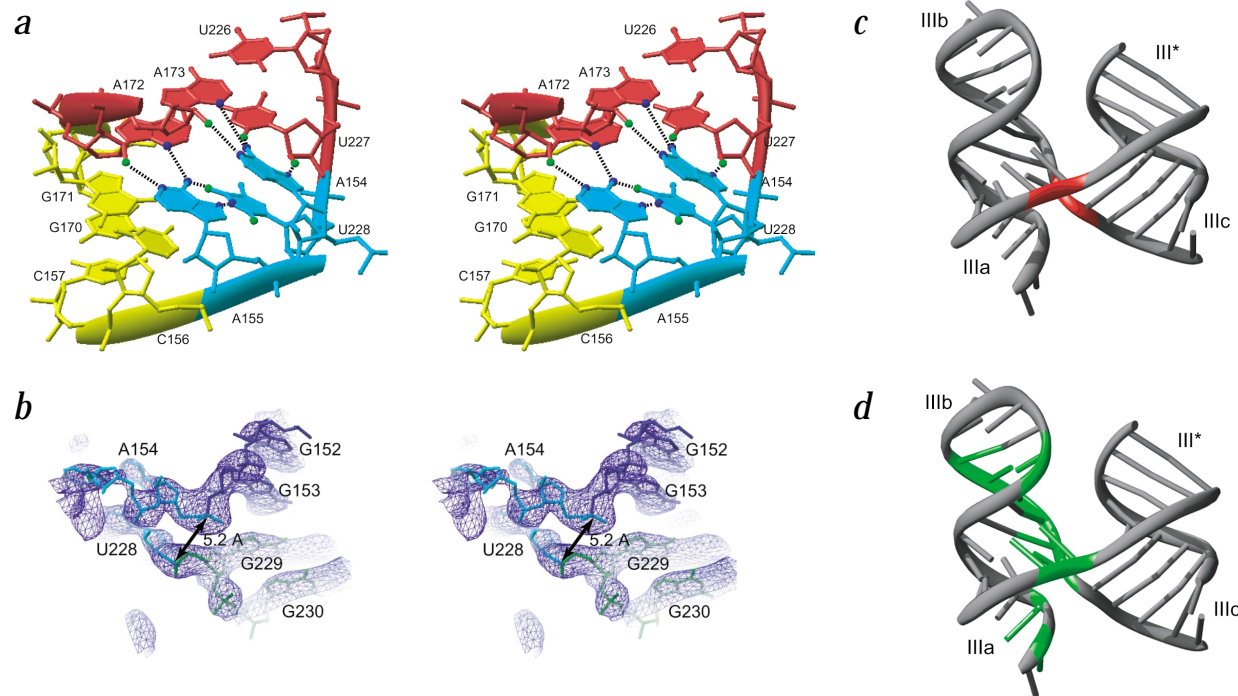


**Fig. 3** Details of the junction structure that contribute to binding site geometry. **a**, Stereo close-up view of the interactions between the junction nucleotides and the minor groove of helix IIIb. Hydrogen bonds are shown as dashed lines, and the color scheme is as Fig. 1b. The gray arrows indicate Watson-Crick base pairs in helix IIIb. **b**, Portion of experimental electron density of the junction, contoured at 2.0  $\sigma$  above the mean. Transition from one stack to the other occurs with a single phosphate linkage. The two phosphates at the crossover are only 5.2 Å apart. **c**, Backbone locations that are protected from Fe(II)-EDTA cleavage in the context of the folded full-length HCV IRES RNA are colored in red on the junction structure. Protections were observed at positions U228, G229, G153, A154 and A155. **d**, Superposition of nucleotide positions identified in a modification interference of eIF3 binding to the full-length HCV IRES RNA. Interferences were observed at A154, A155, U160, A167, U174, U175 (C in crystal construct), A223 (G in crystal construct), G224, A225, U226, U227 and U228. Figure was created using Ribbons<sup>25</sup>.



**Table 1** Translation initiation activity of mutant HCV IRES relative to wild type

Mutant	Activity (%)
A154G	1 ± 1
A155G	3 ± 1
A172U	9 ± 2
A172U/U227A	69 ± 6
A173U	5 ± 1
A173U/U226A	99 ± 20
G171C/C156G	90 ± 14
G170C/C157G	4 ± 1

type levels (Table 1). In stem-loop IIIa, a region implicated in direct eIF3 interaction<sup>9,14,15</sup>, the C157-G170 and C156-G171 base pairs are adjacent to the junction but do not seem to contribute directly to its hydrogen bonding network. Even though reversing the C-G base pair immediately adjacent to the junction results in almost no loss of initiation activity, reversal of base pair C157-G170 results in a significant reduction in translation initiation. Although the loss of initiation activity cannot be readily explained by the crystal structure, changing this base pair may disrupt a critical intermolecular contact with eIF3 or the 40S subunit in stem IIIa.

Because all three junction nucleotides (A154, A155 and U228) lie in the IIIa-IIIb interface, no single-stranded nucleotides bridge the junction between the IIIa-IIIb and IIIc-III\* helical stacks. Rather, there is a 180° turn between U228, which stacks with IIIb, and G229, which stacks with IIIc. Similarly, G153 stacks on III\*, and A154 is displaced 180° to stack on IIIa. This results in a bridge that contains only two phosphate residues and also brings the two helical stacks into close proximity in this region. In addition, the two bridging phosphates are in close proximity, forming a locus of concentrated negative charge (Fig. 3b). Thus, the structure compares favorably with data from hydroxyl radical probing experiments that predicted the collapse of this region into a tight ion-induced fold (Fig. 3c). No metal ions were observed in the electron density map. This is consistent with the observation that folding of the IRES RNA is driven primarily by charge neutralization rather than through formation of highly specific metal ion binding sites<sup>10</sup>.

### eIF3 binding involves a distorted helix

Recognition of an RNA target by a cognate binding protein is often facilitated by the formation of distorted backbone structures and the presentation of specific RNA base functional groups in one of the helical grooves<sup>20</sup>. The displacement of IIIb relative to IIIa and the 180° turn between U228 and G229 creates a distinct kink in the RNA backbone as it passes through the junction. This also brings the backbone of IIIa, in the vicinity of A167, into close proximity with this kink between U228 and G229. Thus, the major groove of the IIIa-IIIb interface is narrowed and the minor groove is opened and accessible. The proposal that these features contribute to forming the recognition surface for eIF3 is supported by the observation that the nucleotides identified by modification interference largely occur within these structural features and not in the more A-form IIIc-III\* stack<sup>9</sup> (Fig. 3d).

### Conclusions

Crosslinking data suggest that the IIIb loop directly contacts subunits of eIF3, an observation supported by the failure of the

truncated IIIabc junction alone to bind eIF3. In contrast, a construct of the intact IIIabc region (which includes loop IIIb) from the HCV IRES binds eIF3 with the same affinity as that obtained for the intact IRES ( $K_d \sim 35$  nM). In the cryo-EM map of the IRES-40S subunit complex, the IIIb stem-loop was tentatively assigned to a region of the IRES density that protrudes from the solvent-exposed 40S subunit surface. Efforts to orient the IIIabc junction crystal structure within the IRES-40S subunit complex were inconclusive because of the modest resolution of the cryo-EM image. However, the IIIabc junction crystal structure provides a basis for modeling the intact IIIabc region that will enable further experimentation to determine how eIF3 contacts the IRES and, ultimately, what role eIF3 plays in internal translation initiation.

### Methods

**RNA transcription and purification.** Plasmids encoding the desired RNA sequences were generated using standard cloning techniques. The insert containing the T7 promoter, the desired RNA sequence and a hepatitis delta virus ribozyme on the 3' end was ligated into the *EcoRI*-*Bam*H1 site of pUC19. Transcription and purification was performed as described<sup>10</sup>.

**Crystallization.** Purified RNA was annealed in 30 mM HEPES-KOH, pH 7.5, by heating to 65 °C for 1 min, cooling at room temperature for 5 min and then adding 2.5 mM MgCl<sub>2</sub> and 1 mM spermidine. The final RNA concentration was 5 mg ml<sup>-1</sup>. The RNA was crystallized by the sitting drop vapor diffusion method by adding 2 μl of macromolecular solution to 4 μl of crystallization solution containing 30% (v/v) 2-methyl-2,4-pentanediol (MPD), 0.1 M sodium citrate, pH 5.6, and 0.2 M ammonium acetate. After 24 h at 30 °C, drops were streak-seeded using a cat whisker and a stock of pulverized crystals in 40% (v/v) MDP, 0.1 M sodium citrate, pH 5.6, and 0.2 M ammonium acetate. Crystals appeared after 1–10 d at 30 °C and grew as plates to a maximum size of 100 μm × 600 μm × 600 μm. Crystals were harvested by transfer into a cryoprotectant solution containing 30% (v/v) MPD, 10% (v/v) isopropanol, 0.1 M sodium citrate, pH 5.6, 0.2 M ammonium acetate, 20 mM MgCl<sub>2</sub> and 5 mM spermine, and flashed cooled in liquid propane. The crystals (space group P4<sub>2</sub>2<sub>1</sub>2) have unit cell parameters  $a = b = 66.5$  Å and  $c = 95.9$  Å, and contain 1 molecule per asymmetric unit, with a mosaic spread of 0.5°.

**Data collection, phase determination and refinement.** Data (Table 2) were collected (MAD data using the inverse beam method) on brominated RNA crystals at 100 K at the National Synchrotron Light

**Table 2** Diffraction data and refinement statistics

Data set	$\lambda_1$	$\lambda_2$	$\lambda_3$	$\lambda_4$
Diffraction data (Å)				
Resolution	50–2.8	50–2.8	50–2.8	50–2.8
Wavelength	0.9204	0.9197	0.9273	0.9020
Reflections				
Total	72,167	72,049	72,854	70,891
Unique	9,652	9,671	9,665	9,592
Completeness (%) <sup>1</sup>	98.3 (95.1)	98.5 (96.2)	98.3 (96.7)	97.5 (90.5)
$\langle I \rangle / \langle \sigma(I) \rangle$ <sup>1</sup>	23.8 (2.5)	23.4 (2.4)	23.5 (3.5)	97.5 (90.5)
$R_{\text{sym}}$ (%) <sup>1,2</sup>	7.8 (53.6)	7.8 (56.3)	7.3 (38.7)	7.5 (49.2)
Phasing statistics				
Phasing power <sup>3</sup>	0.9	2.4	0.1	0.3
$R_{\text{Kraut}}$ <sup>4</sup>	0.05	0.04	0.05	0.05

<sup>1</sup>Numbers in parentheses refer to the highest resolution shell (2.9–2.8 Å).

<sup>2</sup> $R_{\text{sym}} = \sum |I - \langle I \rangle| / \sum I$ , where  $I$  is the observed intensity and  $\langle I \rangle$  is the statistically weighted absolute intensity of several measurements of symmetry-related reflections.

<sup>3</sup>Phasing power =  $\langle |F_{\text{h}}| \rangle / \langle |F_{\text{p}} + F_{\text{h}}| - |F_{\text{ph}}| \rangle$ , reported for all centric reflections.

<sup>4</sup> $R_{\text{Kraut}} = \sum |F_{\text{p}} + F_{\text{h}}| - |F_{\text{ph}}| / \sum |F_{\text{p}}|$ , reported for all reflections.

Source beamline X25, with 10 s exposures and 1° oscillations. Data sets were reduced using DENZO and SCALEPACK<sup>21</sup>. Five bromine sites were located with CNS<sup>22</sup> by averaging the anomalous difference Patterson maps of  $\lambda_1$  and  $\lambda_2$  and the dispersive difference map of  $\lambda_2$ ,  $\lambda_4$ . Heavy atoms sites were refined, and phases obtained to 2.8 Å using  $\lambda_2$  only (overall FOM = 0.5). Density modification and solvent flipping yielded a map in which almost all RNA residues could be built unambiguously (overall FOM = 0.9). The inclusion of data from other wavelengths did not appreciably improve the electron density. O<sup>23</sup> was used to build the initial model.

Rounds of energy minimization, simulated annealing, restrained individual B-factor refinement and manual examination and rebuilding using  $\lambda_1$  and  $\lambda_2$  led to the current model ( $R_{\text{free}} = 28.3$  and  $R_{\text{work}} = 27.9$ ). The final overall B-factor is 55.5 Å<sup>2</sup>, but this is inflated by the high B-factors of the less well-ordered IIIa nucleotides, which exceed 110 Å<sup>2</sup>. The cross-validated  $\sigma_A$  mean coordinate error is 0.48 Å, and the r.m.s deviations from ideal bond lengths and angles are 0.006 Å and 1.22°, respectively.

**Mutagenesis of HCV IRES.** Mutations were introduced into pHCV35.2 (ref. 10) using the QuikChange™ Site-Directed Mutagenesis Kit (Stratagene). To determine the effects of assembled mutations on the translational efficiency of the HCV IRES, an *NcoI*-*StuI* restriction fragment spanning the region was removed from pHCV35.2 and ligated into pT7BR(1B/408)P (same restriction sites)<sup>24</sup>.

**In vitro transcription and translation.** Reactions were carried out as described<sup>9,24</sup>. Briefly, *in vitro* transcription and translation reactions were carried out using the TNT™ T7 Quick coupled transcription-translation system (Promega). Triplicate reaction mixtures (25 µl) were assembled containing 19.5 µl of rabbit reticulocyte lysate (RRL) master mix and 0.5 µl of 1 mM methionine, programmed with 5.0 µl of purified plasmid DNA (0.1 µg µl<sup>-1</sup>) and incubated at 30 °C for 90 min. Reactions were analyzed for RLuc and FLuc reporter activities using the Dual-Luciferase reporter assay system (Promega). Results listed are the average efficiency of each mutation (relative to wild type) from three experiments including the standard deviation (Table 1).

**Coordinates.** Coordinates and structure factors have been deposited in the Protein Data Bank (accession code 1KH6).

## Acknowledgments

The authors wish to thank the NSLS X25 beamline staff and the Yale Center for Structural Biology staff for assistance in data collection and processing. We also thank L. Zhang, D.J. Battle and J.M. Murray for assistance in data collection and figure construction (DB), and A.R. Ferré-D'Amaré, R.T. Batey, R.P. Rambo and P.L. Adams for helpful discussions and advice.

## Competing interests statement

The authors declare that they have no competing financial interests.

Correspondence should be addressed to J.A.D. *email: doudna@csb.yale.edu*

Received 30 November, 2001; accepted 19 February, 2002.

1. Pestova, T.V. *et al. Proc. Natl. Acad. Sci. USA* **98**, 7029–7036 (2001).
2. Hellen, C.U. & Sarnow, P. *Genes Dev.* **15**, 1593–1612 (2001).
3. Tsukiyama-Kohara, K., Iizuka, N., Kohara, M. & Nomoto, A. *J. Virol.* **66**, 1476–1483 (1992).
4. Lemon, S.M. & Honda, M. *Semin. Virol.* **8**, 274–288 (1997).
5. Pestova, T.V., Shatsky, I.N., Fletcher, S.P., Jackson, R.J. & Hellen, C.U. *Genes Dev.* **12**, 67–83 (1998).
6. Sizova, D.V., Kolupaeva, V.G., Pestova, T.V., Shatsky, I.N. & Hellen, C.U. *J. Virol.* **72**, 4775–4782 (1998).
7. Hellen, C.U. & Pestova, T.V. *J. Viral. Hepat.* **6**, 79–87 (1999).
8. Kolupaeva, V.G., Pestova, T.V. & Hellen, C.U. *J. Virol.* **74**, 6242–6250 (2000).
9. Kieft, J.S., Zhou, K., Jubin, R. & Doudna, J.A. *RNA* **7**, 194–206 (2001).
10. Kieft, J.S. *et al. J. Mol. Biol.* **292**, 513–29 (1999).
11. Spahn, C.M. *et al. Science* **291**, 1959–1962 (2001).
12. Klinck, R. *et al. RNA* **6**, 1423–1431 (2000).
13. Lukavsky, P.J., Otto, G.A., Lancaster, A.M., Sarnow, P. & Puglisi, J.D. *Nature Struct. Biol.* **7**, 1105–1110 (2000).
14. Buratti, E., Tisminetzky, S., Zotti, M. & Baralle, F.E. *Nucleic Acids Res.* **26**, 3179–3187 (1998).
15. Odreman-Macchioli, F.E., Tisminetzky, S.G., Zotti, M., Baralle, F.E. & Buratti, E. *Nucleic Acids Res.* **28**, 875–885 (2000).
16. Baugh, C., Grate, D. & Wilson, C. *J. Mol. Biol.* **301**, 117–128 (2000).
17. Ban, N., Nissen, P., Hansen, J., Moore, P.B. & Steitz, T.A. *Science* **289**, 905–920 (2000).
18. Lopez de Quinto, S., Lafuente, E. & Martinez-Salas, E. *RNA* **7**, 1213–1226 (2001).
19. Ho, P.S. & Eichman, B.F. *Curr. Opin. Struct. Biol.* **11**, 302–308 (2001).
20. Leulliot, N. & Varani, G. *Biochemistry* **40**, 7947–7956 (2001).
21. Otwinowski, V. & Minor, W. *Methods Enzymol.* **276**, 307–326 (1997).
22. Brünger, A. *et al. Acta Crystallogr. D* **54**, 905–921 (1998).
23. Jones, T.A., Zou, J.Y., Cowan, S.W. & Kjeldgaard, M. *Acta Crystallogr. A* **47**, 110–119 (1991).
24. Jubin, R. *et al. J. Virol.* **74**, 10430–10437 (2000).
25. Carson, M. *J. Appl. Crystallogr.* **24**, 958–961 (1991).